

A Unified Geometric Model for 3D Confocal Image Analysis in Cytology

A. SARTI, C. ORTIZ, S. LOCKETT AND R. MALLADI

Lawrence Berkeley National Laboratory
University of California
Berkeley, CA 94720. USA
{asarti,malladi}@math.lbl.gov
{carlos,lockett}@black.lbl.gov

Abstract. In this paper, we use partial differential equation based analysis as a methodology for computer-aided cytology. We wish to accurately extract and classify the shapes of nuclei from noisy confocal microscopy images. This is a prerequisite to an accurate quantitative intranuclear (genotypic and phenotypic) and internuclear (tissue structure) analysis of cancerous and pre-cancerous specimens. We study the use of a geometric-driven scheme for improving the results obtained by a nuclear segmentation method, based on automatic segmentation, followed by object reconstruction and interactive classification. We build a chain of methods that includes an edge-preserving image smoothing mechanism, an automatic (albeit non-regularized) segmentation method, a geometry-driven scheme to regularize the shapes and improve edge fidelity, and an interactive method to split shape clusters and reclassify them.

Keywords: Cytology, Image processing, Segmentation, Dynamic surfaces, Level Sets, Differential geometry, Riemannian geometry, Surface evolution

1 Introduction

Cytology shows that the cells in a tissue become increasingly heterogeneous in their structural properties during carcinogenesis, while histology shows increasing disorganization of the cells. Furthermore, whether a pre-cancerous or cancerous lesion progresses, is stable or enters remission is likely to depend on the chemical and physical environment of the cell in the lesion [8][10][18] in addition to the internal properties of the cells. In order to understand these structural alterations, together with the molecular mechanisms underlying them, it is necessary to analyze the cells individually and within their natural tissue context. Since many of the structural and molecular changes occur within the cell's nucleus, the ability to segment the individual nuclei in intact tissue is therefore an important and basic technical capability.

To obtain quantitatively accurate measurements at the individual nucleus level, it is necessary to analyze intact nuclei. Therefore, thick (> 20 micron) sections must be employed, which requires three-dimensional (3D) (confocal) microscopic image acquisition [30] followed by 3D image analysis. In order to facilitate the segmentation of nuclei from images, it is usual to label the specimen with a fluorescent DNA counterstain, because it produces very high contrast images containing high intensity nuclear regions versus low intensity non-nuclear (back-

ground) regions. Actual segmentation of nuclei can be obtained by either interactive or automatic algorithms. Interactive methods, based on drawing around nuclei in sequence [6][22] or orthogonal [11] 2D slices are superior in performance (defined as the fraction of nuclei correctly segmented) based on visual judgement of the results compared to automatic algorithms. However, they are slow, typically taking minutes per nucleus and are thus limited in their practical application to situations where only 10s of nuclei require analysis.

Automatic algorithms [3][9][22], on the other hand are much faster, enabling the analysis of 100s to 1000s of nuclei per study: The performance of the automatic methods is only high ($> 90\%$) for specimens containing isolated nuclei. Performance significantly deteriorates for many cancer specimens, because the cells are structurally dominated by their nuclei leaving little separating cytoplasm and thus the images show clustered nuclei. To overcome that limitation, our 3D segmentation approach combines the performance of interactive algorithms by including visual inspection stages in the approach with the speed of automatic image analysis algorithms, enabling the correct segmentation of a high proportion of individual nuclei in intact tissue. This approach greatly reduces user effort, while providing the same accuracy as the manual method for segmenting cell nuclei stained with a fluorescent DNA dye. Although our

method outperforms the other methods mentioned before, some refinement is still necessary in terms of edge fidelity and segmentation of densely clustered specimens.

Encouraged by the recent advances [13][14] [15]-[16][29][2][23] [26][17] in partial differential equation based image analysis tools, in this paper, we extend and apply some of those methods to confocal microscope image analysis. The theme of this paper is to start with a governing equation that is expressed via an Euler-Lagrange of a functional and to show its many interpretations; these include tasks ranging from edge-preserving image denoising, shape extraction in 3D, curvature based min-flow to rid a given shape of its holes, and to split nuclear clusters in order to re-classify them. Various forms of our equation are then implemented using the level set [21] methods and the efficient narrow-band versions [1][13] of it.

The rest of the paper is organized as follows: in Section 2 we introduce the main equation and we outline its relevant features. In Section 3, we summarize the automatic segmentation method that we employ. In Section 4, we interpret the main equation as an image processing algorithm and show its application to confocal microscope image denoising. In Section 5 we examine the geometric interpretation of the model and show that it can be used for shape refinement and segmentation. In Section 6 we use variations of our main model for cluster classification; specifically, we show how hole elimination can be performed via a curvature based flow, and finally we use a multiple interface version of our geometric model to extract the shapes of nuclei avoiding their merger.

2 Geometric Model for Image Analysis

In this section, we introduce a geometric model; various forms of this equation are used in this paper in order to implement our image analysis procedures. The method relies on estimating the motion of curves and surfaces that move in the normal direction with a given speed. Given a hypersurface $\gamma(\mathbf{x})$ that is moving under speed $F(\mathbf{x})$, we adopt the level set equation to represent its motion [21] [27][28]. In other words, we embed the hypersurface as the zero level set of a higher dimensional function $\psi(\mathbf{x})$, and write the following equation of motion by following chain rule:

$$\psi_t + F |\nabla \psi| = 0, \quad (1)$$

with a given initial condition $\psi(\mathbf{x}, t = 0) = \psi_0$.

This model of curve and surface motion has been applied to the problem of shape modeling in [12][4][13][15]. Imagine that one is given an image and the

problem is to extract boundary descriptions of all the shapes implicitly present in it. The approach in [13] is one of using a trial shape that propagates in the image domain and molds itself into the desired boundary. The speed function used to control this shape recovery process is a combination of constant inflationary speed, a geometry dependent speed that regularizes the final result, and an image-dependent speed. Specifically, the equation of motion is given by,

$$\psi_t + g(1 - \epsilon H) |\nabla \psi| = 0, \quad (2)$$

where g is a decreasing function of the image gradient and H is the mean curvature. An additional forcing term can be added to this equation to improve the accuracy in the presence of large variations in image gradient. This is often realized by advecting the surface along an image dependent vector field [5][15]; the force field is synthesized in such a way that it always points in the edge direction. With this change, our equation becomes

$$\psi_t + g(1 - \epsilon H) |\nabla \psi| - \beta \nabla g \cdot \nabla \psi = 0. \quad (3)$$

This equation is then solved with a user-defined initial condition. The key advantages of our geometric model over other shape recovery schemes is its topological adaptability, robust numerics, and very fast implementations [16].

3 Image Denoising

Low level image analysis presents two basic requirements. One is to smooth all the homogeneous regions that contain noise and the other is to retain in an accurate way the location of the boundaries that define the shape of the represented structures. In bio-medical imaging strong oscillations are due to different causes, in particular to the noise intrinsically present in the acquisition process. The application of traditional pre-processing algorithms (moving average, median and Gaussian filtering) do not reduce the noise superimposed on the image while maintaining a good definition of the edges.

We now show how we can use Eqn. (3) to do image processing. The basic idea is to delete the constant speed term and solve the equation with the noisy image as the initial condition, namely

$$\psi_t = gH |\nabla \psi| + \beta \nabla g \cdot \nabla \psi, \quad (4)$$

with $\psi(\mathbf{x}, t = 0) = I_0(\mathbf{x})$. The first term in the above equation is a parabolic smoothing term and the second is a hyperbolic term. The proposed model is a selective smoothing of the 3D image, where the edges are enhanced and preserved as much as possible. A

contrast function g allows us to decide whether a detail is sharp enough to be kept. In our model, g is a smooth nonincreasing function of the initial image $I_0(x)$, namely

$$g = g(|\nabla(G(x) \otimes I_0(x))|) \quad (5)$$

where $G(x)$ is a Gauss kernel and the symbol \otimes denotes convolution.

In particular, $g(0) = 1$, $g(|\nabla(G(x) \otimes I_0(x))|) \geq 0$, and $\lim_{|\nabla(G(x) \otimes I_0(x))| \rightarrow \infty} g(|\nabla(G(x) \otimes I_0(x))|) = 0$. Typical forms of $g(|\nabla(G(x) \otimes I_0(x))|)$ are:

$$g(|\nabla(G(x) \otimes I_0(x))|) = e^{-\frac{|\nabla(G(x) \otimes I_0(x))|}{\gamma}} \quad (6)$$

or

$$g(|\nabla(G(x) \otimes I_0(x))|) = \frac{1}{1 + \frac{|\nabla(G(x) \otimes I_0(x))|}{\gamma}}. \quad (7)$$

The smoothing works as follows: if $|\nabla(G(x) \otimes I_0(x))|$ is large, the flow is slow and the exact location of the edges will be retained. If $|\nabla(G(x) \otimes I_0(x))|$ is small then the flow tends to be fast thereby increasing the smoothing process. Notice that the filtering model reduces to mean curvature flow when $g(s) = 1$. The second (hyperbolic) term in Eqn. (4) sharpens the edge information in the image; note that a similar observation was made in [24].

The only other parameter we have to fix is the variance of the Gauss kernel. We note that the minimal size of the detail is related to the size of the Gauss kernel, which acts like a scale parameter. In fact the variance of $G_\sigma(x) = \frac{1}{C_\sigma} e^{-\frac{|x|^2}{4\sigma}}$ corresponds to the dimension of the smallest structures that have to be preserved.

Now we present some results. Figure 1(a) is a benign region of a breast cancer specimen, labeled with a fluorescent stain (propidium iodide) for identification of the cell nuclei. The lower bilayer of nuclei are in epithelial cells and are surrounding a duct. Figure 1(b) shows the result of solving Eqn. (4) with the image itself as an initial condition; Figure 2 and 3 show the result of 3D edge-preserving smoothing on a confocal microscope image volume.

4 Automatic Segmentation: A Summary

In this section, we follow some of the work in [20] and briefly summarize the automatic segmentation method to get a rough estimate of nuclear shapes.

1. First a rough estimation of the nuclei size was calculated for every image, since that value was used in subsequent steps. A Hough Transform based algorithm was applied to estimate it.

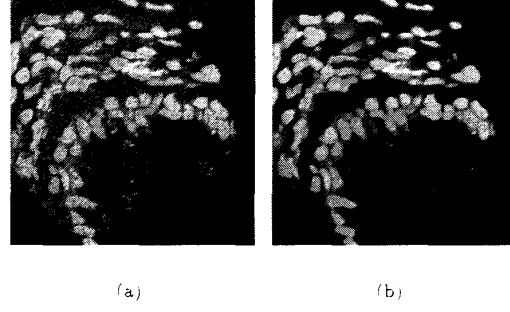
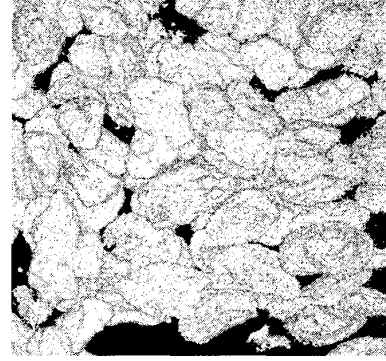
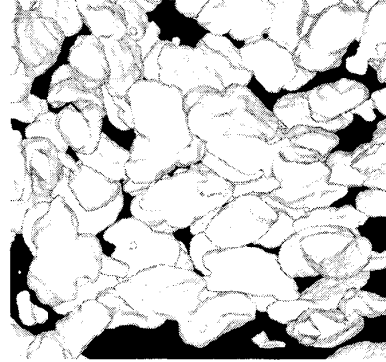


Figure 1: 2D edge-preserving smoothing and edge sharpening results; (a) 2D slice of the unfiltered image, and (b) Geometric image processing with $\beta = 1$ and $\sigma = 1$.

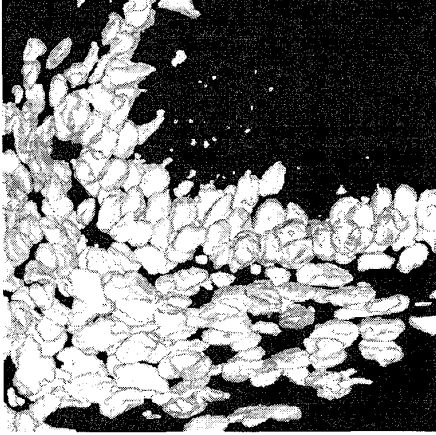


(a)



(b)

Figure 2: 3D edge-preserving smoothing and edge sharpening results; (a) Surface rendering representation of the unfiltered volume, and (b) Geometric image processing with $\beta = 1$ and $\sigma = 1$.



(a)

Figure 3: Geometric image processing of an entire volume of cells.

2. An adaptive, gradient-weighted thresholding algorithm was used to separate nuclear areas from the image background.
3. The binary image obtained after thresholding the initial image was filtered to remove small objects and to divide slightly touching clusters of objects. To do that, the image was eroded and then a background skeleton was calculated to find surfaces among the objects. Those surfaces were imposed on the original binary images, so they defined edges of slightly touching objects.
4. The individual objects were labeled, interpolated, measured and converted into an object-type structure that contains the object measurements and both the binary and gray level information of each object. Then objects were linked in a hierarchical ordered list. This object-oriented step reduced the amount of information to be handled in the following steps.
5. Objects were rendered and visualized using a software called daVinci (Data Visualization'N Computer Interaction). The user went through the list of objects generated by the segmentation algorithm. All objects were originally unclassified, so the user classified them as Nucleus, Cluster of Nuclei or Debris. Classification is performed by clicking on a button. Divided nuclei, if any, were rejoined.
6. Objects classified as clusters of nuclei were divided into individual nuclei using a watershed-based algorithm. The strategy was as follows: first we calculated the Vector Distance Transform of the binary object. Then we Gaussian-filtered the distance and applied a morphological peak extraction based in the gray-scale image reconstruction algorithm. These peaks were used as makers for the watershed. We used the original gray values as the flooding surface for the watershed, so the watershed accurately delineated the surface of minimum intensity between nuclei.
7. After cluster segmentation, the resulting object were measured and linked to the input list, and the user classified them again.

5 Segmentation and Shape Refinement

As shown in Figure 4(a), the resulting surfaces from our automatic segmentation algorithm can be quite coarse with a lot of “voxelization”. In addition, the shape boundaries shown may also be a little away from the true edges. We wish to correct this by refining the shapes using the geometrical flow introduced in previous sections. To that end, let us revisit Eqn. (3), from the geometrical point of view of achieving boundary detection.

Assume that the surface \mathcal{S} is a particular level set of a function $\psi : [0, a] \times [0, b] \times [0, c] \rightarrow R$. In other words, \mathcal{S} is a set of points at which the function ψ is equal to a given constant. The embedding function ψ can therefore be considered as an implicit representation of the surface \mathcal{S} .

It is easy to prove that if a surface \mathcal{S} evolves according to

$$\mathcal{S}_t = F\vec{\mathcal{N}} \quad (8)$$

where $\vec{\mathcal{N}}$ is the unit inward normal and F is a real function, then the level set function ψ obeys the following evolution rule

$$\psi_t = F|\nabla\psi|; \quad (9)$$

see [21][27] for details.

In order to smooth a surface, we can let the speed F be equal to its mean curvature H . The flow decreases the total curvature and has the property of “smoothing out” all the high curvature regions on the surface, i.e. local variations [7]. However, this flow will also destroy useful surface features if run long enough. One of the main issues concerning this flow is if there is a natural stopping criterion for an optimal shape refinement. Several methods have been proposed in the past, one that adds a term to force

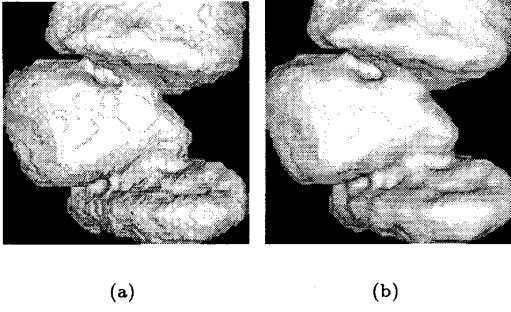


Figure 4: Shape refinement; (a) Zero level set of the signed distance function computed on the rough segmentation of a cluster of cells, and (b) Geometric segmentation with $\beta = 1$ and $\sigma = 1$

the solution to remain close to the initial data [19], and the authors in [14] have studied a scale dependent stopping criteria implemented via a min – max curvature flow. In the present context, the stopping condition is given by the g function. So, the surface moves according to the equation

$$S_t = gH\vec{N}. \quad (10)$$

We now rewrite Eqn. (3) without the constant speed term here:

$$\psi_t - gH |\nabla\psi| - \beta\nabla g \cdot \nabla\psi = 0, \quad (11)$$

where β is a non-zero constant. The first term smooths the surface while keeping it close to the edges and the second term, $\beta\nabla g \cdot \nabla\psi$, attracts the surface closer to the edge map. The initial condition $\psi(\mathbf{x}, t = 0)$ is given by the signed distance function computed off of the binarized image obtained from a rough segmentation. The result of applying this flow on a coarse binary segmentation is shown in Figure 4.

6 Interactive Cluster Segmentation

As mentioned in the introduction, in some cancer specimens, the cells are structurally dominated by their nuclei and the resulting images show clustered nuclei. From our segmentation standpoint this means that there is not enough delineating image gradient information to tell two adjacent nuclei apart. Therefore, we have to now consider the problem of segmenting a cluster into a set of isolated nuclei. In this section, we are going to examine how to split the cluster into single cells and then consider how to reconstruct the exact shape of each cell. The easiest

way to split the cluster is to use the morphological operator of *erosion*. In the PDE parlance, this can be achieved via the level set flow on the cluster surface under a speed $F = -1$, namely

$$\psi_t = |\nabla\psi|; \quad (12)$$

reader is referred to [25] for related work. Unfortunately the structure of a cluster is not always compact because it can contain several holes inside. Therefore the *erosion* flow acts like a shortening flow for the external boundaries, but it expands the internal holes thereby corrupting the basic shape itself. To prevent this effect we have to first eliminate the holes. We can achieve this task by performing a *closing* operation, in the sense of the mathematical morphology, by a flow that provides sequentially a *dilation* and an *erosion* effect. In the context of level set flow, the *closing* operation is achieved by considering two flows, $F = 1$ to obtain *dilation* and subsequently $F = -1$ for *erosion*.

In practice however, the *dilation* operation has to be performed carefully in order to avoid the merger of two close but distinct clusters thus complicating the problem further. For that reason, we use a more sophisticated flow for hole elimination. This eliminates holes and is bounded by the convex hull of the original cluster. Specifically, the flow is given by

$$\psi_t = \min(H, 0.0)|\nabla\psi|. \quad (13)$$

This flow in 2D has been used recently in [14] in the context of image denoising and for surface smoothing in [15]. We have simply replaced the Euclidean curvature that was used for 2D image processing with the mean curvature in 3D. The main feature of the flow is that it allow the inward concave regions to grow outwards, while suppressing the motion of the outward convex regions. Thus the evolving shape always remains inside the convex hull. The holes are thus subject to a mean curvature flow while the outer shape converges to its convex hull. In Figure 5 we show a 2D example of hole elimination via $\min(K, 0)$ flow and in Figure 6, we show the result of hole elimination in a cropped sample of a nuclear cluster.

We notice from Figure 6 that hole elimination sometimes compromises the shape detail. In other words, the cell shapes stray away from high image gradients. We amend the loss in accuracy by solving our shape refinement equation, i.e. Eqn. (3), for a few time steps. Note that the image based component in the equation – the g function – is computed from the enhanced image. This procedure results in a cluster that is devoid of any holes and close to the “true” edges present in the image; the shape after this step is shown in Figure 7.

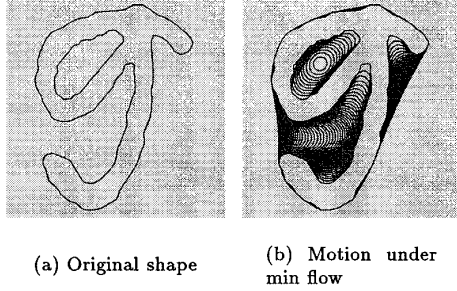
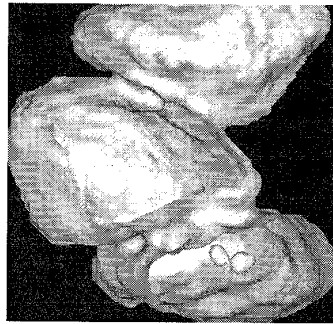
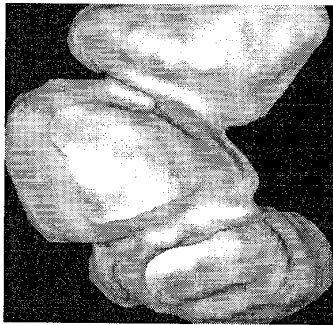


Figure 5: 2D example of hole elimination with a $\min(K, 0)$ flow. Note that the outer shape converges to its convex hull.

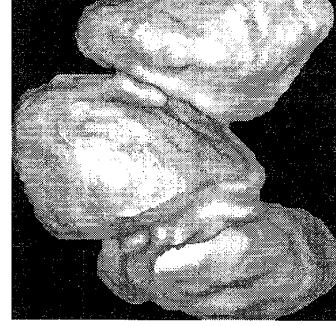


(a)



(b)

Figure 6: Hole elimination: (a) zero-level set of the refined shape. The volume has been cropped to reveal two internal holes. (b) The shape after 10 iterations of the min flow. The holes disappear, but the shape loses detail.



(a)

Figure 7: The refined shape without holes after the geometric flow processing.

6.1 Multiple interface flow

After the hole removal and shape refinement we can proceed to shrink the cluster until single nuclei emerge as topologically distinct objects. The main point of this section, is how to grow them back to their original shape while maintaining their distinct identity. If we propagate the individual (nucleus) shape models according to Eqn. (3), they will be attracted to image edges but will merge into a cluster upon colliding with each other. That is exactly the behavior we wish to avoid. Instead, we would like the individual shapes to grow and segment the nucleus shapes, touch in areas where there is not enough delineating image gradient information, but never merge.

A similar problem arises when one tries to study the motion of multiple interfaces propagating in the same domain [28]. We follow the same idea here in order to build a scheme that moves shapes in a distinct manner. First, we build a separate level set function for each shape. Next, each shape is advanced to obtain a trial value for each level set function with the following geometrical flow

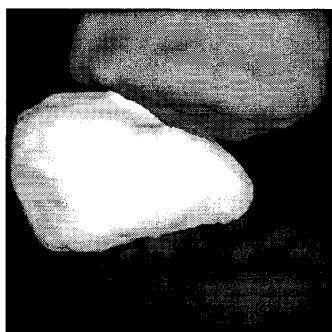
$$\frac{\partial \phi_i}{\partial t} = \nabla(g(|\nabla I_0|) \nabla \frac{\nabla \phi_i}{|\nabla \phi_i|}), \quad (14)$$

where ϕ_i is the level set function for the i -th shape. If two regions collide based on the trial function values, the value of the actual function is changed by considering the values of other level set functions. Merger can be avoided by a simple max operator. Further details can be found in [28].

We now present the result of cluster reclassification. Figure 7 shows the initial cluster (without



(a)



(b)

Figure 8: The refined clusters after processing with the multiple interface flow; (a) three distinct shapes after the *erode* operation; (b) three different cells have been recognized and segmented.

holes) that we know from visual inspection contains three nuclei merged into one. Figure 8(a) is the result of shrinking the shape until it splits into three separate parts. These shapes are then evolved separately under the same image based g function using the multiple interface update rules; the result is shown in Figure 8(b). The three shapes shown in different colors segment three distinct nuclei.

Acknowledgements

This work was supported under Contract No. DE-AC03-76SF00098 of the U.S. Department of Energy's Office of Energy Research, Office of Computational and Technology Research, Mathematical, Information, and Computational Sciences Division, Applied Mathematical Sciences Subprogram; Director, Of-

fice of Energy Research, Office of Health and Environmental Research; and LBNL Directed Research and Development Program. This work was also supported by the U.S. National Institute of Health Grant CA-67412, a contract with Zeiss Inc., and by the Training program in Genome Research of the UC Systemwide Biotechnology Research and Education Program.

References

- [1] D. Adalsteinsson and J. A. Sethian, "A fast level set method for propagating interfaces," in *J. Comp. Phys.*, Vol. 118(2), pp. 269-277, May 1995.
- [2] L. Alvarez, F. Guichard, P. L. Lions, and J. M. Morel, "Axioms and fundamental equations of image processing," *Arch. Rational Mechanics* **123**, 1993.
- [3] H. Ancin, B. Roysam, T.E. Dufresne, M. M. Chesnut, G. M. Ridder, D. H. Szarowski, J. N. Turner, "Advances in Automated 3-D Image Analysis of Cell Populations Imaged by Confocal Microscopy," *Cytometry* **25**, pp.221-234, 1996.
- [4] V. Caselles, F. Catte, T. Coll, F. Dibos, "A geometric model for active contours," *Numerische Mathematik*, Vol. 66, pp. 1-31, 1993.
- [5] V. Caselles, R. Kimmel, and G. Sapiro, "Geodesic active contours," in *Proc. ICCV'95*, Cambridge, MA 1995.
- [6] Czader M., Liljeborg A., Auer G., Porwit A., "Confocal 3-Dimensional DNA Image Cytometry in Thick Tissue Sections," *Cytometry* **25**, pp.246-253, 1996.
- [7] M. Grayson, "The heat equation shrinks embedded plane curves to round points," *J. Differential Geometry* **26**, 1987, pp. 285-314.
- [8] G. H. Heppner "Cell-to-cell interaction in regulating diversity of neoplasms," *Seminars in Cancer Biology*, **2**, pp. 97-103, 1991.
- [9] Irinopoulou T., Vassy J., Beil M., Nicolopoulou P., Encaoua D., Rigaut J.P., "Three-Dimensional DNA Image Cytometry by Confocal Scanning Laser Microscopy in Thick Tissue Blocks of Prostatic Lesions," *Cytometry*, pp. 27:99-105, 1997.
- [10] Lelievre S., Weaver V.M., Bissell M.J., "Extracellular matrix signaling from the cellular membrane skeleton to the nuclear skeleton: A model

- of gene regulation", *Recent Progress in Hormone Research* **51** pp. 417-432, 1996.
- [11] Lockett S.J., Sudar D., Thompson C.T., Pinkel D., Gray J.W., "Efficient, interactive, three-dimensional segmentation of cell nuclei in thick tissue sections", *Cytometry*, **31**, pp. 275-286, 1998.
 - [12] R. Malladi, J.A. Sethian, B.C. Vemuri, "A topology-independent shape modeling scheme," in *SPIE: Geometric Methods in Computer Vision II*, Vol. 2031, pp. 246-258, 1993.
 - [13] R. Malladi, J. A. Sethian and B. C. Vemuri, "Shape modeling with front propagation: A level set approach," *IEEE Trans. on PAMI* **17**, 1995, pp. 158-175.
 - [14] R. Malladi and J. A. Sethian, "Image processing: Flows under Min/Max curvature and mean curvature," in *Graphical Models and Image Processing*, Vol. 58(2), pp. 127-141, March 1996.
 - [15] R. Malladi and J. A. Sethian, "Level set methods for curvature flow, image enhancement, and shape recovery in medical images," in *Visualization and Mathematics: Experiments, Simulations, and Environments*, Eds. H. C. Hege, K. Polthier, pp. 329-345, Springer Verlag, Heidelberg, 1997.
 - [16] R. Malladi and J. A. Sethian, "A real-time algorithm for medical shape recovery," in *Proceedings of ICCV '98*, pp. 304-310, Mumbai India, January 1998.
 - [17] K.Mikula, A.Sarti, C.Lamberti "Geometrical diffusion in 3D echocardiography", *Proc. of ALGORITMY '97- Conference on Scientific Computing*, West Tatra Mountains, Slovakia, 1997.
 - [18] Miller F.R., Heppner G.H. "Cellular interactions in metastasis", *Cancer and Metastasis Reviews* **9**, pp. 21-34, 1990.
 - [19] N. K. Nordstrom, "Variational edge detection," *PhD dissertation*, Department of electrical engineering, University of California, Berkeley, 1990
 - [20] C. Ortiz de Solorzano, E Garcia Rodriguez, A. Jones, D. Pinkel, J.W. Gray, D. Sudar, and S.J. Loeckett, "Segmentation of confocal microscope images of cell nuclei in thick tissue sections," submitted to the *Journal of Microscopy*, 1998.
 - [21] S. J. Osher and J. A. Sethian, "Fronts propagation with curvature dependent speed: Algorithms based on Hamilton-Jacobi formulations," *Journal of Computational Physics* **79**, 1988, pp. 12-49.
 - [22] Rigaut J.P., Vassy J., Herlin P., Duigou F., Masson E., Briane D., Foucrier J., Carvajal-Gonzalez S., Downs A.M., Mandard A-M., "Three-Dimensional DNA Image Cytometry by Confocal Scanning Laser Microscopy in Thick Tissue Blocks", *Cytometry*, **12**, pp. 511-524, 1991.
 - [23] Bart M. ter Haar Romeny(Ed.) *Geometry-driven diffusion in computer vision*, Kluwer Academic Press, 1994.
 - [24] G. Sapiro, "Color snakes," Hewlett-Packard Lab. tech report, 1995.
 - [25] G. Sapiro, R. Kimmel, D. Shaked, B. B. Kimia, and A. M. Bruckstein, "Implementing continuous-scale morphology via curve evolution," *Pattern Recognition*, Vol. 26(9), pp. 1363-1372, 1993.
 - [26] A.Sarti, K.Mikula, F.Sgallari "Nonlinear multiscale analysis of 3D echocardiographic sequences", Submitted to *IEEE Trans. on Medical Imaging*, 1997.
 - [27] J. A. Sethian, "A review of recent numerical algorithms for hypersurfaces moving with curvature dependent flows," *J. Differential Geometry* **31**, 1989, pp. 131-161.
 - [28] J. A. Sethian, *Level set methods: Evolving interfaces in geometry, fluid mechanics, computer vision, and material science*, Cambridge University Press, 1997.
 - [29] N. Sochen, R. Kimmel, and R. Malladi, "A General Framework for Low Level Vision," in *IEEE Transactions on Image Processing*, special issue on PDEs and Geometry-Driven Diffusion in Image Processing and Analysis, Vol. 7, No. 3, pp. 310-318, March 1998.
 - [30] T. Wilson, *Confocal Microscopy*, Academic Press, London, 1990.